This paper is published as part of a PCCP Themed Issue on:
Metal oxide nanostructures: synthesis, properties and applications

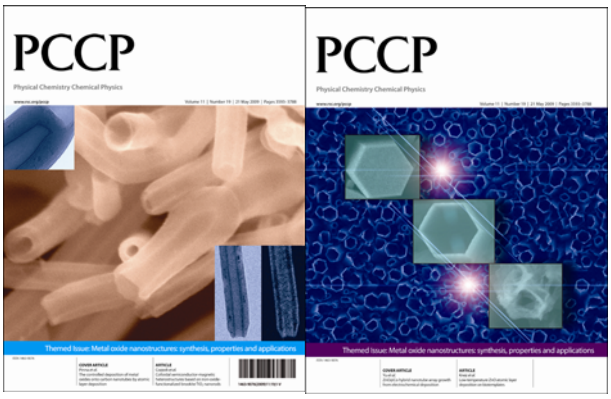

Guest Editors: Nicola Pinna, Markus Niederberger, John Martin Gregg and Jean-Francois Hochepied

Editorial

Papers

Thin-walled Er^{3+}:Y_2O_3 nanotubes showing up-converted fluorescence
Christoph Erk, Sofia Martin Caba, Holger Lange, Stefan Werner, Christian Thomsen, Martin Steinhart, Andreas Berger and Sabine Schlecht, *Phys. Chem. Chem. Phys.*, 2009
DOI: 10.1039/b821304f

Wettability conversion of colloidal TiO_2 nanocrystal thin films with UV-switchable hydrophilicity
Gianvito Caputo, Roberto Cingolani, Pantaleo Davide Cozzoli and Athanassia Athanassiou, *Phys. Chem. Chem. Phys.*, 2009
DOI: 10.1039/b823331d

Nucleation and growth of atomic layer deposition of HfO_2 gate dielectric layers on silicon oxide: a multiscale modelling investigation
A. Dkhissi, G. Mazaleyrat, A. Estève and M. Djafari Rouhani, *Phys. Chem. Chem. Phys.*, 2009
DOI: 10.1039/b821502b

Designing meso- and macropore architectures in hybrid organic–inorganic membranes by combining surfactant and breath figure templating (BFT)
Ozlem Sel, Christel Laberty-Robert, Thierry Azais and Clément Sanchez, *Phys. Chem. Chem. Phys.*, 2009
DOI: 10.1039/b821506e

The controlled deposition of metal oxides onto carbon nanotubes by atomic layer deposition: examples and a case study on the application of V_2O_4 coated nanotubes in gas sensing
Marc-Georg Willinger, Giovanni Neri, Anna Bonavita, Giuseppe Micali, Erwan Rauwel, Tobias Herntrich and Nicola Pinna, *Phys. Chem. Chem. Phys.*, 2009
DOI: 10.1039/b821555c

***In situ* investigation of molecular kinetics and particle formation of water-dispersible titania nanocrystals**
G. Garnweitner and C. Grote, *Phys. Chem. Chem. Phys.*, 2009
DOI: 10.1039/b821973g

Chemoresistive sensing of light alkanes with SnO_2 nanocrystals: a DFT-based insight
Mauro Epifani, J. Daniel Prades, Elisabetta Comini, Albert Cirera, Pietro Siciliano, Guido Faglia and Joan R. Morante, *Phys. Chem. Chem. Phys.*, 2009
DOI: 10.1039/b820665a

Colloidal semiconductor/magnetic heterostructures based on iron-oxide-functionalized brookite TiO_2 nanorods†

Raffaella Buonsanti,[ab] Etienne Snoeck,[c] Cinzia Giannini,[d] Fabia Gozzo,[e] Mar Garcia-Hernandez,[f] Miguel Angel Garcia,[gh] Roberto Cingolani[bi] and Pantaleo Davide Cozzoli*[ab]

Received 8th December 2008, Accepted 5th February 2009
First published as an Advance Article on the web 5th March 2009
DOI: 10.1039/b821964h

A flexible colloidal seeded-growth strategy has been developed to synthesize all-oxide semiconductor/magnetic hybrid nanocrystals (HNCs) in various topological arrangements, for which the dimensions of the constituent material domains can be controlled independently over a wide range. Our approach relies on driving preferential heterogeneous nucleation and growth of spinel cubic iron oxide (IO) domains onto brookite TiO_2 nanorods (*b*-TiO_2) with tailored geometric parameters, by means of time-programmed delivery of organometallic precursors into a suitable TiO_2-loaded surfactant environment. The *b*-TiO_2 seeds exhibit size-dependent accessibility towards IO under diffusion-controlled growth regime, which allows attainment of HNCs individually made of a single *b*-TiO_2 section functionalized with either one or multiple nearly spherical IO domains. In spite of the dissimilarity of the respective crystal-phases, the two materials share large interfacial junctions without significant lattice strain being induced across the heterostructures. The synthetic achievements have been supported by a systematic morphological, compositional and structural characterization of the as-prepared HNCs, offering a mechanistic insight into the specific role of the seeds in the control of heterostructure formation in liquid media. In addition, the impact of the formed *b*-TiO_2/IO heterojunctions on the magnetic properties of IO has also been assessed.

1. Introduction

Over the past decades, remarkable progress in many fields of nanoscience has been boosted by the availability of colloidal inorganic nanocrystals (NCs) with finely tailored composition and geometric parameters. They have served both as model systems for authenticating the laws of low-dimensional solids, and as easily processable building blocks for the realization of innovative materials, devices and processes.[1] Although refinement in the dimensional/morphological features of NCs is still desirable, a further challenging research direction has recently emerged in the area of synthetic nanochemistry, which aims at enhancing the structural and topological complexity of wet-chemically prepared nano-objects in order to both expand and diversify their technological potential. Advanced generations of multi-component nanoheterostructures, henceforth referred to as hybrid NCs (HNCs), are being pursued, which individually comprise two or more sections of different inorganic materials permanently assembled through direct bonding interfaces without any molecular bridges.[2–5] So far, HNCs have been engineered in various elaborate topologies, spanning from core/shell and yolk/shell geometries, to oligomer-like architectures made of shape-tailored material domains sharing limited contact junctions.[2–5] HNCs with a spatially controlled distribution of their crystal-phase constituents are expected to respond to the growing demand for "smart" nanoentities on which not only multiple optoelectronic, magnetic and/or catalytic functionalities can be simultaneously exploitable, but also exchange-coupling or electronic communication effects among joint material sections may give rise to novel chemical–physical behaviour, not otherwise achievable with any of the single constituents alone.[2–5]

The synthesis of HNCs represents an extremely challenging task. On one side, thermodynamic and kinetic processes underlying the size and shape evolution of the constituent domains need to be regulated for different materials. On the

[a] *Scuola Superiore ISUFI, Università del Salento, Distretto Tecnologico ISUFI via per Arnesano km 5, 73100, Lecce, Italy. E-mail: davide.cozzoli@unile.it; Fax: +39 0832 298238; Tel: +39 0832 298231*
[b] *National Nanotechnology Laboratory of CNR-INFM, Unità di Ricerca IIT via per Arnesano km 5, 73100, Lecce, Italy*
[c] *CEMES-CNRS, 29 rue Jeanne Marvig, B.P. 94347, 31055, Toulouse Cedex, France*
[d] *Istituto di Cristallografia (IC-CNR), via Amendola 122/O, 70126, Bari, Italy*
[e] *Swiss Light Source, Paul Scherrer Institute, 5232, Villigen PSI, Switzerland*
[f] *Instituto de Ciencia de Materiales de Madrid, CSIC C/ Sor Juana Ines de la Cruz 3, Campus de Cantoblanco, 28049, Madrid, Spain*
[g] *Department of Material Physics, University Complutense, 28024, Madrid, Spain*
[h] *Instituto de Ceramica y Vidrio, CSIC, C/ Kelsen 5 Campus de Cantoblanco, Madrid, 28049, Spain*
[i] *Istituto Italiano di Tecnologia (IIT), via Morego 30, 16163, Genova, Italy*

† Electronic supplementary information (ESI) available: Fitting of SR-XRD patterns (supplementary Fig. S1–S3); statistical TEM analysis of samples investigated by SQUID (supplementary Fig. S4). See DOI: 10.1039/b821964h

other side, creation of inorganic junctions between dissimilar lattices depends on the ability to regulate the surface–interface energy balance in liquid media by controlling heterogeneous nucleation, facet-preferential chemical reactivity, crystal-phase segregation, and/or solid-state atomic diffusion mechanisms, depending on the specific material association targeted and on the synthetic techniques adopted.[2,3]

Development of HNCs incorporating metal oxides promises to open interesting technological opportunities, due to the incredibly rich variety of solid-state properties that characterize this class of materials on the nanoscale. However, although a relatively large library of heterostructures made of various combination of semiconductor, metal and magnetic compounds has been already accessed, nevertheless the available selection of all-oxide based HNCs remains quite poor.[2] Examples include mainly core/shell configurations of MnO/Mn_3O_4,[6] $CoFe_2O_4/MnO$,[7] $CoFe_2O_4/Fe_3O_4$,[8] Fe_3O_4/SiO_2[9–12] and ZnO/MgO,[13] and a few prototypes of non-onionlike systems, namely SiO_2-encapsulated Fe_3O_4–PdO heterodimers,[14] and ZnO and TiO_2 nanorods decorated with either titania[15] or iron oxide domains,[16] respectively. Such a limited level of synthetic expertise with which oxides can be combined in the form of HNCs clearly poses the urgency to devise novel preparation techniques as well as to gain deeper insight into the mechanisms governing heterostructure formation in the liquid phase.

In the present work we address the colloidal fabrication of semiconductor/magnetic heterostructures based on two relevant oxide materials, namely TiO_2 and iron oxide (IO), whose nanoscale association can be envisioned to enable exploitation of technologically valuable multifunctional capabilities. TiO_2/IO based HNCs could benefit numerous environmental and biomedical applications, in the form of magnetically recoverable adsorbent and (photo)catalyst platforms, on one side,[17–21] and as tools for analytical separations,[22–24] drug delivery,[22,23,25–27] diagnostics[24,26] and therapeutics (*e.g.* gene and cancer cell therapy), on the other side.[28–30] As of today, progress in this field is yet hindered by the difficulty to realize TiO_2/IO architectures beyond the conventional nanocomposite systems, in which the spatial distribution of the two materials and their crystallographic relations cannot be controlled.[21,31–33]

A powerful and widely exploited strategy for engineering HNCs in the liquid phase relies on the so-called seeded growth, whereby preformed foreign NC seeds act as primary low-energy nucleation centres onto which secondary inorganic portions of different materials can be grown from the respective molecular precursors. Recently, this technique has been used to develop highly strained binary HNCs,[16] each composed of a short rod-like TiO_2 portion with one IO spherical particle epitaxially attached to any location of its longitudinal sidewalls. Such HNCs were specifically seeded with TiO_2 nanorods in the tetragonal anatase phase (henceforth referred to as *a*-TiO_2) derived by a low-temperature hydrolytic route.[34] The constituent materials in such *a*-TiO_2/IO HNCs were lattice-distorted, while sharing a small and locally curved junction regions in response to interfacial mismatch as high as ~13%. The intense strain fields induced across such heterostructures permitted each *a*-TiO_2 seed substrate to accommodate only a single IO domain, further dictating the ultimate size (~15–17 nm) to which the latter could be grown.[16]

As a matter of fact, for TiO_2/IO HNCs to meet suitable requirements in applications in which a particularly efficient magnetic response and optimized catalytic activity are desired, a significant leap forward in their synthetic design should be made. The ability to independently tailor the domain sizes of the respective material components, to extend their upper dimensional limits, as well as to equip individual TiO_2 sections with multiple magnetic IO portions, are among the most important goals that need to be achieved.

Here, we describe a versatile colloidal seeded-growth approach to novel TiO_2/IO HNCs, by which strain-related heteroepitaxial growth constraints can be greatly overcome, thereby allowing for the synthesis of heterostructures in various topological arrangements and with geometric parameters tuneable over a wide dimensional interval. Our key strategy relies on directing the growth of IO in the inverse spinel cubic structure by means of TiO_2 NRs selectively tailored in the orthorhombic brookite crystal phase (henceforth referred to as *b*-TiO_2). Unlike their *a*-TiO_2 counterparts,[34] such *b*-TiO_2 seeds exhibit size-dependent accessibility towards IO under a diffusion-controlled growth regime, which is realized upon application of time-programmed delivery of an organometallic iron precursor to a calibrated *b*-TiO_2-loaded surfactant environment. Such reaction dynamics translates into unique flexibility in the preparation of HNCs individually made of a *b*-TiO_2 section functionalized with either one or multiple nearly spherical IO domains, whose respective dimensions can be tailored almost independently. These synthetic achievements are supported by a systematic morphological, compositional and structural characterization of the as-prepared HNCs, offering a mechanistic insight into the specific role of the seeds in driving heterostructure formation in liquid media. In addition, the impact of the *b*-TiO_2/IO heterojunction formation on the magnetic properties of IO is also investigated.

2. Experimental

2.1 Synthesis procedures

Materials. All chemicals were of the highest purity available and were used as received, titanium(IV) chloride ($TiCl_4$, 99.999%), iron pentacarbonyl ($Fe(CO)_5$, 98%), dodecan-1,2–diol ($C_{12}H_{24}(OH)_2$ or DDIOL, 90%), oleic acid ($C_{17}H_{33}CO_2H$ or OLAC, 90%), oleyl amine ($C_{17}H_{33}NH_2$ or OLAM, 70%), and 1-octadecene ($C_{18}H_{36}$ or ODE, 90%) were purchased from Aldrich. All solvents used were of analytical grade.

Preparation of TiO_2 nanorod seeds. All the syntheses were carried out under air-free conditions using a standard Schlenk line setup. Brookite TiO_2 nanorods (*b*-TiO_2 NRs) with tuneable sizes were synthesized by a recently developed procedure with minor modifications.[35] Briefly, 3 g of ODE, 50 mmol of OLAM and 1 mmol of OLAC were loaded into a three-neck flask and degassed at 120 °C for 30 min, after which the mixture was cooled down to 50 °C under N_2 flow. At this point, 1 mmol of $TiCl_4$ was added, and the flask was heated up to 290 °C at a ramp rate of ~20 °C min^{-1}. As the temperature

was increased, the solution turned from colourless to pale yellow, to dark brown, and finally to a milky white. After heating for 30 min at 290 °C, the reaction could be either halted by removing the heating mantle and allowing rapid cooling, or continued upon addition of a room-temperature secondary feedstock precursor solution of equimolar $TiCl_4$: OLAC (0.5 M in ODE) at a constant rate of 0.1 mL min^{-1} by means of a syringe pump (GENIE Plus Syringe Pump, Kent Scientific). Progressively larger NRs were obtained by injecting increasing amounts of the $TiCl_4$: OLAC mixture (up to an additional 25 mmol of $TiCl_4$) to the initial mixture.

After the synthesis, the *b*-TiO_2 NRs were extracted and purified under ambient atmosphere. The TiO_2 product was separated from its growing mixture upon co-addition of 2-propanol and acetone and subsequent centrifugation (5000 rpm), after which they were thoroughly washed with acetone to remove precursor and surfactant/ODE residuals. The purified NRs were used to prepare stable *b*-TiO_2 NRs seed stock solutions in $CHCl_3$, whose concentrations were checked by ICP-AES analysis prior to further use.

Synthesis and purification of TiO_2/IO HNCs. The synthesis of the HNCs was purposely adapted from literature protocols.[16,30] Appropriate amounts of the *b*-TiO_2 seeds (0.1–1 mmol expressed in TiO_2 molecular units), DDIOL, OLAM, and OLAC were mixed with 10 mL of ODE in a three-neck flask. The mixture was pumped to vacuum for 30 min at 120 °C, after which it was heated up under N_2 flux to 280 °C. Then, 1 mL of a room-temperature 0.1–1 M $Fe(CO)_5$ solution in previously degassed ODE was injected in a single portion (in less than 0.1 s) to the vigorously stirred *b*-TiO_2-contaning mixture. In all the synthesis, the initial $Fe(CO)_5$: OLAC : OLAM : DDIOL molar ratio was set at 1 : 1.5 : 0.75 : 1.25, while the TiO_2 : $Fe(CO)_5$ molar ratio could be varied from 1 : 2 to 1 : 10. The $Fe(CO)_5$ injection caused a temperature drop of ~20–40 °C, after which the temperature was allowed to slowly recover to the initial value. The onset of iron oxide nucleation was characterized by an induction time of 1–2 min, marked by a sudden darkening of the solution, which was inversely proportional to the amount of $Fe(CO)_5$ injected. After heating for 1 h at 280 °C, the reaction could be either halted or continued upon delivering an additional 2–10 mL of $Fe(CO)_5$–OLAC–ODE feedstock precursors (0.5 M, prepared in a separated flask under N_2 with a Fe:OLAC molar ratio of 1 : 1.5) at a rate of 0.1 mL min^{-1} by means of a syringe pump (GENIE Plus Syringe Pump, Kent Scientific). After completion of precursor reaction, the mixture was allowed to cool down to 80 °C and exposed to air for an additional 1 h.

The HNCs were separated from their growing mixture upon 2-propanol addition and subsequently subjected to repeated cycles of re-dissolution in $CHCl_3$ and precipitation with acetone to wash out surfactant residuals. The final hydrophobic-capped HNCs were soluble in a variety of non-polar solvents (such as hexane, toluene, or chloroform).

Monitoring heterostructure growth. The temporal evolution of nanoheterostructure growth was monitored by performing TEM analyses on aliquots of the hot surfactant mixture extracted *via* a glass syringe at scheduled time intervals. The aliquots were suddenly cooled down and eventually subjected to extraction/purification procedures, as described above.

2.2 Characterization

Elemental analysis. The Ti and Fe atomic content of nanocrystal samples was measured by inductively coupled plasma atomic emission spectroscopy (ICP-AES) measurements with a Varian Vista AX spectrometer. The samples for analyses were digested in concentrated HCl–HNO_3 (3 : 1 v/v). The concentration of TiO_2 and IO were expressed in terms of TiO_2 and Fe_2O_3 (or Fe_3O_4) molecular units.

X-Ray diffraction (XRD). Synchrotron radiation X-ray diffraction (SR-XRD) experiments on dried nanocrystal powders were performed at the Swiss Light Source Materials Science beamline. Full diffraction patterns (60 degrees in 2θ) were collected using the MYTHEN I detector, a fast solid state silicon 1-D detector developed at the Paul Scherrer Institute.[37] Acquisition times were 10 s per pattern. The photon energy was set at 24.2 keV to reduce the effect of fluorescence emission from the sample on the detector performances. The energy was carefully calibrated using NIST Silicon 640 C powder. The instrumental function was found negligible over the intrinsic contribution to the reflection lineshape of all powders investigated. All SR-XRD experiments were performed in Debye–Scherrer (transmission) geometry. The nanocrystal powders were loaded into 0.4 mm capillaries and spun at approximately 10 Hz to improve the count statistics.

Quantitative phase analysis (QPA) of SR-XRD patterns was performed with a whole profile pattern fitting program Quanto[38] based on the Rietveld method. The samples were described as mixtures of different phases: anatase (space group *I*41/*amd*; unit cell parameters: $a = b = 3.7852$ Å, $c = 9.5139$ Å), brookite (space group *Pbca*; unit cell parameters: $a = 9.166$ Å, $b = 5.411$ Å, $c = 5.149$ Å), and maghemite (space group $P4_32_12$, unit cell size: $a = b = c = 8.3457$ Å) or magnetite (space group *Fd*-3*m*; unit cell size: $a = b = c = 8.2686$ Å). The whole diffraction pattern was given by the sum of the background level and the Bragg-diffracted intensity of each crystalline phase, weighted according to phase weight fractions derived from refined scale parameters. The peak intensity was computed by the crystal structure model (chemical species and atomic position in the unit cell). The background was described by a Young polynomial with refinable coefficients. In order to take into account the nanocrystal shape anisotropy, an empirical function was implemented into Quanto to model variations of both peak width and shape as a function of 2θ and *hkl* indices.[39] The accuracy of the weight fraction evaluation was estimated by a goodness-of-fit statistical indicator (GoF), which takes the value of 1 for an ideal fit. Given the high count rate of the pattern intensity, GoF values of <6–7 were considered to be satisfactory. The error in the calculated phase fraction values was about 5–7%.

Transmission electron microscopy (TEM). Low-magnification TEM images were recorded with a Jeol Jem 1011 microscope operating at an accelerating voltage of 100 kV. Statistical size determinations were performed by examining 200 particles in

low magnification TEM images with a dedicated software (Axio Vision). Phase-contrast high-resolution TEM (HRTEM) measurements were performed with Tecnai F20 microscope (FEI) working at an accelerating voltage of 200 kV and equipped with a spherical aberration corrector (CEOS). The microscope point resolution is 0.12 nm. The crystallographic data used for structure determination were the same as those used for XRD analyses. Quantitative analysis of HRTEM images was performed by a geometric phase analysis (GPA) methodology, as described elsewhere.[40,41]

Magnetic measurements. Magnetic measurements were performed on dried nanocrystal powder samples using a MPMS Quantum Design SQUID magnetometer. For comparison purposes, the samples corresponding to TiO_2/IO physical mixtures were prepared by co-mixing appropriate volumes of solutions of purified NRs and separately synthesized IO NCs, and inducing their co-precipitation upon alcohol addition. Samples were always handled with plastic tools and gloves to avoid any possible contamination with metallic particles. For each sample, a new sample holder was used.

3. Results and discussion

The strategy developed here for the preparation of *b*-TiO_2/IO HNCs relies on a two-step seeded-growth scheme that combines the following concepts: (a) exploitation of non-hydrolytic reaction pathways to synthesize organic-capped *b*-TiO_2 NRs with uniform shapes and geometric parameters tuneable over a wide size range; (b) selection of purified NRs with predetermined dimensions as primary seed substrates exhibiting size-dependent reactivity towards IO deposition; (c) induction of preferential heterogeneous nucleation and growth of IO domains onto the seeds in a suitably composed surfactant environment by means of a technique based on carefully regulated injection of an organometallic iron precursor.

3.1 Synthesis and characterization of TiO_2 seeds

The procedure exploited to synthesize *b*-TiO_2 NR seeds involves OLAM-driven aminolysis of titanium carboxylate complexes that are generated *in situ* upon reaction of $TiCl_4$ in OLAC–OLAM–ODE mixtures at 290 °C under inert atmosphere.[35] An initial heating of the complete reaction mixture triggers nucleation and anisotropic growth of TiO_2, while subsequent delivery of additional $TiCl_4$: OLAC feedstock precursors at judiciously slow rate allows steady enlargement of the nanostructures under a continuous unidirectional development regime. Brookite formation and stabilization has been rationalized as arising from the interplay of kinetic and thermodynamic factors, among which the time-variation of the chemical potential for the monomer species in the solution, and the size-dependence of the relative stability of TiO_2 polymorphs in the presence of dynamically surface-adhering surfactants.[5,17,35] The low-magnification TEM overviews in Fig. 1 demonstrate the level of size-morphological control achievable in *b*-TiO_2 synthesis by the selected nonhydrolytic route. The reported results refer to syntheses in which the absolute $TiCl_4$ and OLAC amounts have been systematically

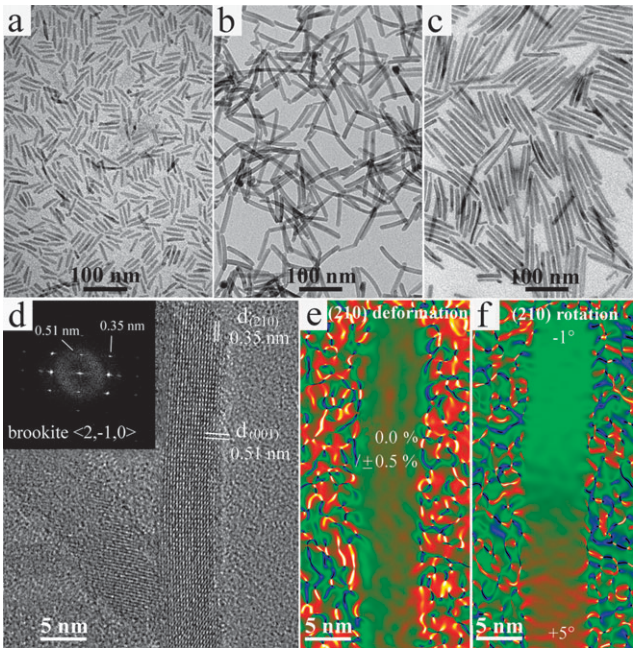

Fig. 1 (a–c) Low-magnification TEM overview of *b*-TiO_2 NR seeds with different geometric parameters synthesized in OLAM–OLAC–ODE mixtures by reacting a total amount of 4, 15 and 25 mmol of $TiCl_4$, respectively. (d) HRTEM image and corresponding FFT (in the inset) of an individual [0,0,1]-elongated brookite TiO_2 NR viewed down the $\langle 2,-1,0\rangle$ zone axis. Characteristic lattice spacings of brookite are also identified. (e–f) False-color deformation and rotation maps, respectively, obtained by GPA analyses of the *b*-TiO_2 (210) lattice fringes visible in the HRTEM image in panel d.

increased at a fixed OLAM content in the reaction environment. The slow heating of the primary $TiCl_4$-loaded surfactant mixture yields oblate TiO_2 objects (Fig. 1a), which can gradually grow to NRs exhibiting a rectangular-like profile with slight longitudinal curvature (Fig. 1b–c). The presence of OLAM at relatively high concentration has been clarified to be essential to promote such morphological evolution under continuous supply of additional precursors.[35] By adjusting the experimental conditions, a systematic tuning of the diameter and the length sizes is achieved in the 3–10 nm and 30–200 nm intervals, respectively, which corresponds to NRs with aspect ratio spanning from ~7–8 to ~15 (Fig. 1b–c).

The crystal-phase composition of the NRs has been confirmed by means of SR-XRD analysis of powdered samples. The representative pattern in part a of Fig. 2 displays remarkable line broadening, in agreement with the formation of nanosized crystalline domains. The profile can be safely indexed to the orthorhombic brookite structure, as suggested by the emergence of the characteristic (121), (022) and (221) reflections and by the shift of all major peaks towards slightly higher angles than those which would otherwise match with the tetragonal anatase reference. Alterations in the relative intensity and widths of various peaks, compared to those associated with the standard pattern of bulk brookite, can be preliminary interpreted as a signature of shape anisotropy. These assignments have been supported by a satisfactory QPA fitting of the experimental data, which has been accomplished

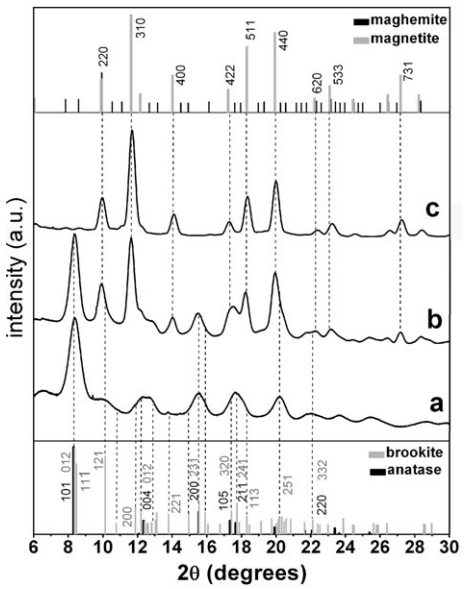

Fig. 2 Representative SR-XRD patterns of: (a) ~5 nm × ~50 nm *b*-TiO_2 NR seeds; (b) *b*-TiO_2/IO HNCs, grown from such NR seeds, which are functionalized with IO domains of ~10 nm; (c) pure IO NCs of ~10 nm synthesized independently. The percentage *b*-TiO_2/spinel cubic IO phase compositions of sample in curve *b*, estimated by fitting the pattern with the QUANTO software, was 65/35, in good agreement with the results of ICP-AES analyses.

by means of an appropriate software program based on the Rietveld method[38] (Fig. S1 in the ESI†).

Phase-contrast HRTEM investigations, along with the fast Fourier transform (FFT) of the relevant images, provided detailed information on the as-synthesized seeds. As highlighted in Fig. 1d, the NRs are indeed single-crystalline objects made of brookite TiO_2 with a preferential lattice elongation in the *c*-axis direction. The NR surface arrangement is generally dominated by the presence of regularly smooth (2,1,0)-type longitudinal facets and by less developed (102)/(001)-type facets at the apex regions, in good agreement with recent theoretical surface energy calculations.[42] In frequent cases, the structure of the nano-objects is complicated by noticeable longitudinal bending and/or subtle lattice distortion (as inferred from changes in the relative fringe intensities along the rod section), which can result in enhancement of the visibility of kinematically forbidden periodicities[35] (*e.g.* the (001) fringes are indeed detectable in Fig. 1d).

In order to assess the presence of lattice strain in the seeds with deeper accuracy, which is relevant to the understanding of their role in the process of IO overgrowth, quantitative GPA of the HRTEM images has been performed.[40,41] This methodology allows variations in the periodicities of the HRTEM contrast to be detected *via* analysis of the local components in the Fourier transform of the image. Eventual effects related to deformations (*i.e.*, to changes in lattice parameters) and/or rotations (*i.e.*, variations in the angular plane development direction) of selected fringes in the two-dimensional projected lattice can be evaluated with respect to an ''unstrained'' area of the nanostructure lattice taken as reference. The results are translated into false-color maps in which areas featured by a given periodicity in the HRTEM contrast are depicted with the same color. Fig. 1e–f reports the results of GPA analysis that has been carried out by considering the detectable (210) fringes of the NR shown in Fig. 1d. The TiO_2 deformation map (Fig. 1e) reveals that there are only negligible alterations (*i.e.*, within ±0.5%) in the spacing of the selected (210) planes as they span the entire NR section. Differently, the rotation map (Fig. 1f) evidences a curling of the (210) planes across the long axis (as can be already grasped from the HRTEM image itself), which gives rise to the visible longitudinal curvature. The relative degree of bending, measured across opposite regions of the NR, ranges from about −1% to +5%.

3.2 Synthesis of TiO_2/IO HNCs

The HNCs have been prepared by a seeding approach, whereby preformed *b*-TiO_2 NRs, henceforth referred to as the ''seeds'', act as substrate catalysts onto which the growth of secondary IO inorganic portions can be preferentially directed under suitable conditions. To this aim, an appropriate seed-loaded surfactant environment has been composed by co-dissolving calibrated amounts of thoroughly purified *b*-TiO_2 NRs, OLAM, OLAC, and DDIOL in optimized relative proportions in ODE at 280 °C under inert atmosphere. An organometallic precursor delivery technique has been then applied, which consists of an initial fast addition of a $Fe(CO)_5$/ODE solution to the seed-containing mixture, followed by secondary supply of comparatively diluted $Fe(CO)_5$/OLAC/ODE feedstock at controllably slow rate. IO is generated by pyrolysis of iron carboxylate (Fe-OLAC) complexes that are formed *in situ*.[36]

The TEM gallery in Fig. 3 demonstrates the topological variety achievable by seeding IO growth with *b*-TiO_2 NR seeds possessing different geometric features (the relevant reactions conditions are summarized in Table 1). On the basis of TEM contrast variations that distinguish them, the as-synthesized composite nano-objects can be preliminarily interpreted as being indeed HNCs that individually incorporate a single rod-like *b*-TiO_2 section and nearly spherical IO domains accommodated at any relative position along its longitudinal sidewalls. These assignments, consistent with the different electron densities that characterize the respective materials, are in accordance with the known reaction pathways of Fe-OLAC complexes in hot surfactant media,[36] as well as with our control experiments that confirm the structural/morphological stability of *b*-TiO_2 seeds under the typical reaction conditions (in the absence of the molecular iron source). The results highlight that heterostructure syntheses exploiting NRs with diameter/length smaller than 4–6 nm/50–60 nm most exclusively yield binary HNCs, *i.e.*, made of a single IO domain attached to each seed (Fig. 3a–d). In general, a decrease in the nominal TiO_2 to $Fe(CO)_5$ concentration ratio leads to formation of proportionally larger IO domains. The latter can be selectively enlarged from ~5 up to ~30–40 nm, while maintaining a narrow size distribution, by continuous delivery of the secondary $Fe(CO)_5$–OLAC–ODE precursor solution after the initial fast injection step (*cf.* Fig. 3a–b, and Fig. 3c–d, respectively). By comparison, an increasingly pronounced tendency toward the formation of high-order

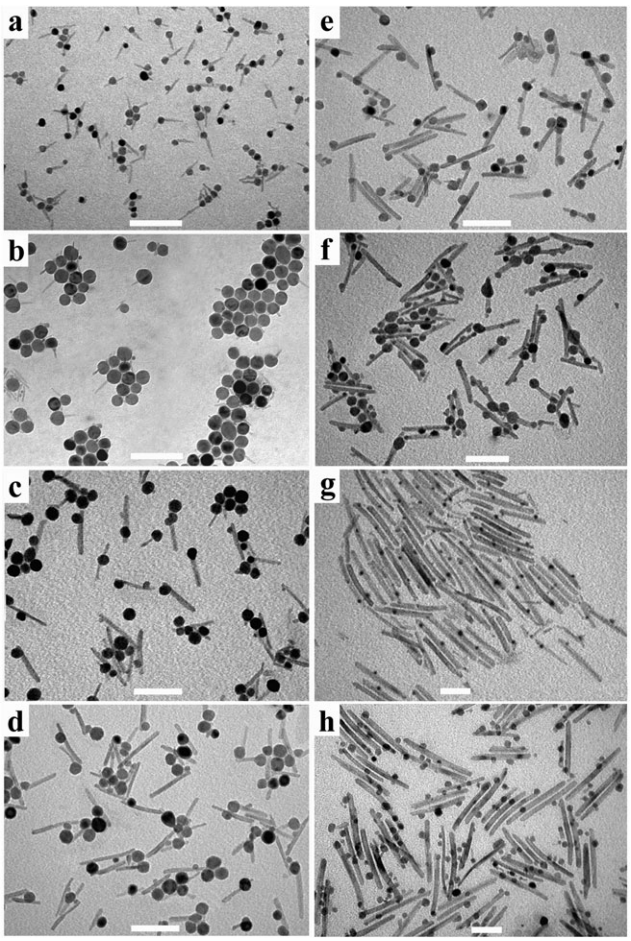

Fig. 3 Low-magnification TEM overviews of HNCs synthesized in OLAM–OLAC–DDIOL–ODE mixtures upon reacting *b*-TiO_2 seeds of different sizes and aspect-ratios with different amounts of organometallic iron precursors, as summarized in Table 1 (white scale bar = 100 nm).

HNCs, *i.e.*, comprising multiply IO-decorated NRs, can be achieved when heterostructure synthesis is seeded with *b*-TiO_2 NRs possessing diameter/length sizes in the 6–10/80–200 nm range (Fig. 3e–h). For a given seed dimension, both the average number of IO domains nucleated on each NR and the relative fraction of high-order HNCs relative to binary heterostructures in the sample population are found to increase as the initial $Fe(CO)_5$: TiO_2 molar ratios realized by the fast injection step are proportionally higher. Similar to what just described earlier, the IO portions can be grown to larger dimensions upon supply of additional precursors, however at the cost of a moderate broadening of their size dispersion (*cf.* Fig. 3e–f and Fig. 3g–h, respectively). In all circumstances, judging from the composition of the particle population, the HNCs are achieved with yields better than 92–95%, thus indicating that parasitic homogeneous nucleation of free-standing IO NCs in the bulk reaction medium is largely suppressed during the entire synthesis course.

The formation of heterostructures, in which *b*-TiO_2 and IO portions are permanently connected, is supported by the fact that the observed domain arrangements can be neither obtained by spontaneous assembly of mixtures of independently prepared *b*-TiO_2 NRs and IO NCs, nor disrupted by any standard post-synthesis processing (*e.g.* repeated cycles of precipitation/redissolution). In addition, whenever required, the HNCs can be selectively size-sorted from the samples by combining alcohol-induced precipitation with magnet-assisted recovery, which proves that the heterostructures indeed represent the objects with the highest mass in the particle population and are magnetically responsive.

Taken together, the experimental data presented above demonstrate that combining accurately size- and shape-tailored *b*-TiO_2 NR seeds (by means of the selected non-hydrolytic protocol) with time-controlled iron precursor addition provides high flexibility in the engineering of *b*-TiO_2/IO heterostructures with tuneable geometric and topological features. A similar opportunity was in fact prohibited when hydrolytically prepared anatase NRs were instead employed as seeds.[16]

3.3 Characterization of TiO_2–IO HNCs

The structural/compositional details of the heterostructures have been investigated by combining SR-XRD and phase-contrast HRTEM analyses.

In the representative XRD pattern reported in part b of Fig. 2 the profile of the initial *b*-TiO_2 NR seeds is convoluted with the characteristic reflections of nanosized IO in the inverse spinel cubic phase of magnetite (Fe_3O_4) and/or maghemite (γ-Fe_2O_3), which are equally found for IO NCs synthesized in the absence of TiO_2 (part c in Fig. 2). The two IO polymorphs can not be discriminated due their close structural similarity and the significant line broadening.[16,36] The crystal-phase composition derived from the corresponding QPA fitting indicate that the brookite structure of the seeds is retained during the course of the HNC synthesis (Fig. S2 and S3 in the ESI†). The agreement with the chemical composition deduced indirectly by ICP-AES measurements is found to be within 5–6%, hence, within the standard deviation error of the QPA fitting procedure.

Table 1 Reaction parameters used in the synthesis of the HNCs shown in Fig. 3

	Sample correspondence with images in Fig. 3							
	Panel a	Panel b	Panel c	Panel d	Panel e	Panel f	Panel g	Panel h
TiO_2 seeds:								
Short axis /nm	5–6	5–6	7–8	7–8	10–12	10–12	12–14	12–14
Long axis/nm	50–55	50–55	80–85	80–85	120–125	120–125	200–210	200–210
TiO_2 in the flask/mmol	0.1	0.1	0.2	0.2	0.4	0.4	1.0	1.0
$Fe(CO)_5$ added by the primary fast injection/mmol	0.5	0.5	1	1	1	1	1.5	1.5
$Fe(CO)_5$ added by the secondary slow injection/mmol	—	4	—	2	—	2	—	2

Fig. 4 and Fig. 5 illustrate HRTEM investigations performed on HNCs with different geometric features. The FFT of the images and identification of relevant lattice distances (Fig. 4a,e and Fig. 5a,e, respectively) confirm that the heterostructures retain one of the original *b*-TiO_2 NR into their elongated section, while the spherical portions are indeed made of single-crystalline IO in the inverse spinel cubic structure of maghemite and/or magnetite (which cannot be distinguished due to subtle differences in the respective lattice spacings), in accordance with the XRD results. As preliminarily suggested by the low-magnification TEM galleries (Fig. 3), the HRTEM inspection clarifies that the IO and the *b*-TiO_2 portions are arranged in various relative configurations. Comparatively larger IO domains are generally found to share proportionally extended interfacial areas with the respective substrates (Fig. 4a,e), either being accommodated on their sidewalls or even embedding a substantial part of NR seed (Fig. 5a,e).

In most cases, the particular orientations under which the *b*-TiO_2 and IO lattices are captured do not allow identification of any coincident crystallographic relationships between them. Neither the angles between the relevant sets of lattice planes of the respective materials, which are most frequently encountered, exhibit constant values in different heterostructures, which points to nonepitaxial growth. Information on lattice strain has been gained by quantitative GPA of HRTEM images.[40,41] The deformation maps relative to the *b*-TiO_2 sections (Fig. 4b,f and Fig. 5b,f, respectively) and the IO domains (Fig. 4d,h and Fig. 5d,h, respectively), evidence that there are no prominent relative variations (*i.e.*, within ±2%) in the spacing of the projected lattice planes. On the other side, the *b*-TiO_2 rotation maps (Fig. 4c,g and Fig. 5c,g, respectively) show a certain degree of curvature across the NR sections, which ranges from −1% to + 5–10%, regardless of the sizes of

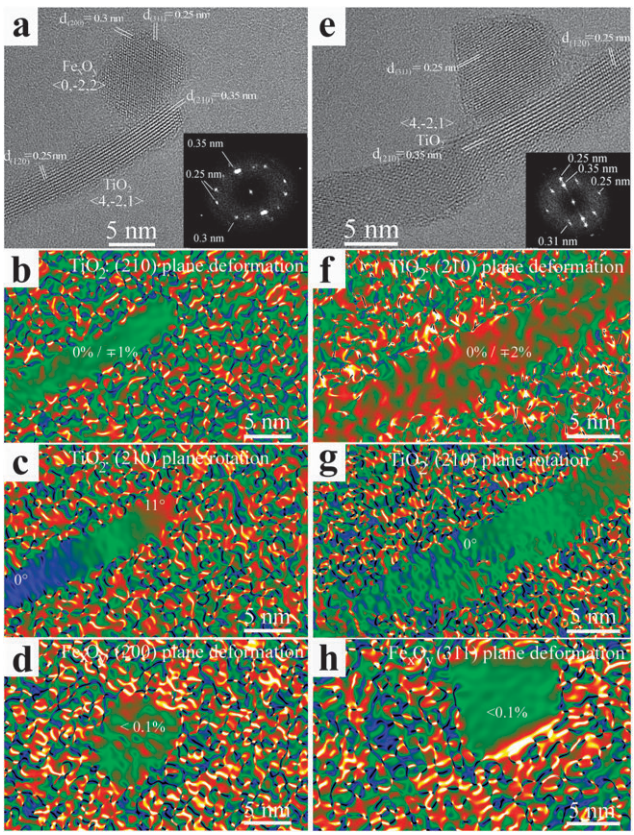

Fig. 4 (a, e) HRTEM images and corresponding FFTs (in the insets) of portions of individual *b*-TiO_2/IO HNCs grown on medium-sized seeds and carrying 8–10 nm IO domains. The relevant zone axes and lattice spacings of the respective materials are also identified. (b, f) False-color deformation and (c, g) rotation maps of the rod-like sections, obtained by GPA analyses of the (210) *b*-TiO_2 lattice fringes visible in the HRTEM images in panels a and e, respectively. (d, h) False-color deformation maps of the spherical domains, obtained by GPA analyses of the (311) IO lattice fringes detectable in the HRTEM images in panels a and e, respectively.

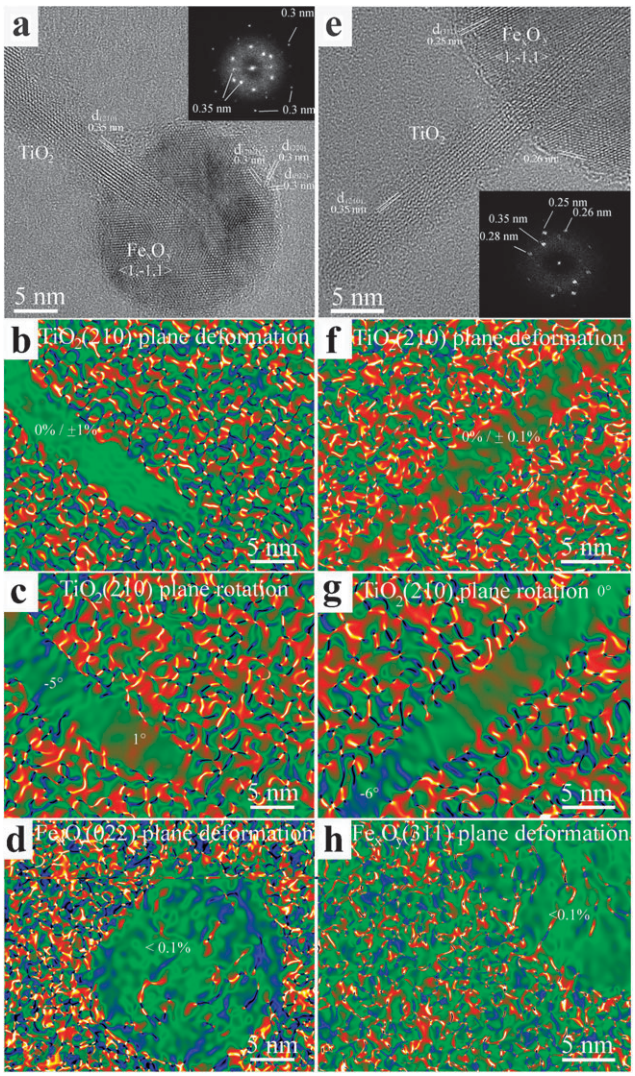

Fig. 5 (a, e) HRTEM images and corresponding FFTs (in the insets) of portions of individual *b*-TiO_2/IO HNCs grown on medium-sized seeds and carrying 15–30 nm IO domains. The relevant zone axes and lattice spacings of the respective materials are also identified. (b, f) False-color deformation and (c, g) rotation maps of the rod-like sections, obtained by GPA analyses of the (210) *b*-TiO2 lattice fringes visible in the HRTEM images in panels a and *e*, respectively. (d, h) False-color deformation maps of the spherical domains, obtained by GPA analyses of the (022) and (311) IO lattice fringes detectable in the HRTEM images in panels a and e, respectively.

the IO domains attached and the extension of the intervening heterointerfaces. Notably, such values are generally of the same order as those found for the starting *b*-TiO_2 seeds.

Overall, from the above GPA investigations it clearly emerges that IO overgrowth onto the NRs proceed without causing additional lattice distortion both in the *b*-TiO_2 and the IO sections to any significant extent. Therefore, induction and propagation of extra strain fields across the heterostructures as a consequence of heterojunction formation can be safely assumed to be negligible. These findings diverge considerably from what was instead found for their *a*-TiO_2/IO heterostructure counterparts.[16]

3.4 Mechanism of heterostructure formation

Examination of the synthesis products at various stages of their formation reveals that the HNCs originate through direct deposition, *i.e.*, heterogeneous nucleation and growth, of IO onto the *b*-TiO_2 seeds. This mechanism is indeed supported by the observation that the relative percentage of heterostructures within the total particle population remains high and invariant over the entire synthesis course, while the IO domains grow to gradually larger sizes over time. Accordingly, pertinent control experiments confirm the impossibility of inducing controlled coalescence among *b*-TiO_2 NRs and preformed IO NCs (synthesized independently) as they are forced to react with each other in typical synthesis environments.

The facile size tuning achieved for IO demonstrates that appropriate control of solution supersaturation by time-programmed precursor supply guarantees steady growth of the domains primarily implanted onto the NRs, while circumventing both reiteration of delayed heterogeneous nucleation events and undesired production of separate IO NCs from homogeneous nucleation in the bulk reaction medium.

The key for preparing topologically controlled *b*-TiO_2/IO HNCs in high yields relies on achieving independent control over the fundamental nucleation and the growth processes underlying heterostructure formation. This is realized by using preformed TiO_2 NRs as catalyst seeds, on one side, and by regulating the chemical potential of the reactive monomers in the solution to controllably low levels, on the other side. The seeded-growth scheme transcribes a fundamental concept of the classical nucleation theory (CNT), according to which the activation energy required for one additional foreign material to deposit heterogeneously onto pre-existing NCs is considerably lower than the barrier that has to be overcome to trigger homogeneous nucleation of new crystalline embryos from the respective molecular precursors.[2,3,5] Here, the synthetic potential of the seeded approach is fully realized upon exploiting an organometallic route to generate IO monomers, which is conveniently characterized by a delayed nucleation/fast growth dynamics.[36] During thermal treatment of $Fe(CO)_5$–OLAC–OLAM mixtures (in the absence of any seeds), the monomers which contribute to nucleation IO are distinct from those which participate in the growth stage, and the two processes are characterized by dissimilar temperature dependence.[36] This ultimately leads to a burst of delayed (*i.e.*, after an induction period) homogeneous nucleation, which self-arrests and is followed by autocatalytic growth of the initially generated nuclei in a diffusion-controlled regime. Our synthetic strategy to HNCs profits from such temporally separated homogeneous nucleation and growth stages, which naturally underlies IO generation by the surfactant-assisted route adopted here. Indeed, in a suitably diluted monomer environment containing pre-existing NRs, heterogeneous nucleation of IO on such TiO_2 seeds can be strongly preferred over homogeneous nucleation.[2–5,16]

The time-programmed iron precursor supply sequence that has been exploited for HNC preparation plays an important role. On one side, the primary fast-injection step leads to a sudden temporary increase in solution supersaturation, which provides the system with the extra energy necessary to surpass the barrier for heterogeneous nucleation, while preventing it from approaching the threshold for parasitic homogeneous nucleation to take place. On the other side, subsequent delivery of additional reactants at a judiciously slow rate guarantees a suitably low level of monomers in the solution, which drives exclusive growth of the IO domains. Ultimately, the size-dependent reactivity of the seeds, as well as their relative concentration with respect to $Fe(CO)_5$, dictate the relative balance of monomer consumption between the heterogeneous nucleation and the growth processes. It can be easily rationalized that, for a given availability of reactive iron species, the smaller the total number of seed sites onto which IO nucleates, the higher the monomer concentration left to feed the domains initially formed, which will therefore grow to comparatively larger dimensions. Overall, the seed-mediated synthesis dynamics ultimately accounts for the high yield with which the HNCs can be prepared, as well as for the size control achievable over the IO components.

The interesting dependence of HNC growth mode (*i.e.* average number per NR and the relative location of the IO domains on the NRs) on geometric features of the seeds deserves further discussion. In fact, the CNT takes into account neither the facet-dependence of NC surface energy (being influenced by surfactant adhesion) nor possible insurgence of strain effects due interfacial lattice misfit at the relevant heterojunctions.[2–5]

First, it should be considered that the inherent shape anisotropy of TiO_2 NRs could be expected to kinetically favour deposition of IO onto specific locations of the seeds (*e.g.*, onto the apexes), which correspond to the facets with the highest chemical reactivity (*e.g.* due to their inherent structure and/or inefficient surfactant passivation).[2–5,15,43] Second, the preference of IO to nucleate on certain seed sites could be also driven by the comparatively higher degree of TiO_2/IO lattice matching achievable thereon.[2–5,15] Nevertheless, reiteration of multiple IO deposition events may be disfavoured by the propagation of strain fields across the heterostructure, which could intensify as pre-existing mismatched IO domains grow to larger sizes and share increasingly larger interfaces with TiO_2 underneath.[2,3,16,43] Third, the formation of one IO domain on a given NR facet could result in a polarization charge at the interface between the two materials arising from the higher average electron density of IO relative to TiO_2. Consequent electron enrichment over other IO-free TiO_2 facets may affect deposition of additional IO domains thereon.[2–5]

As a matter of fact, no site-preferential IO nucleation has been observed in our syntheses, indicating that the various crystal facets exposed are almost equally accessible under the applied reaction conditions. Also, the relative spatial arrangement of the respective material lattices is not featured by any recurring crystallographic relationships. More interestingly, the b-TiO_2 seeds can accommodate remarkably large IO domains as well as sustain multiple nucleation events. Despite the strong dissimilarity between the crystal structures and lattice parameters of IO and b-TiO_2, no significant structural distortions have been detected in the HNCs, regardless of dimensional/topological features and of the extension of the shared interfaces. Overall, these results diverge substantially from those found for previously developed a-TiO_2/IO prototype HNCs that could be exclusively obtained in binary configuration with IO sizes smaller than 15–17 nm at the cost of extreme mismatch-induced deformation in both material sections.[16,34]

The formation of HNCs can be more accurately interpreted in terms of energy balance. The observed regime of partial IO "wetting" of the b-TiO_2 seed substrates, in which IO segregates in distinct domains rather than uniformly covering the NR surfaces, is reminiscent of the Volmer–Weber growth mode known in classical heteroepitaxy fabrication techniques.[44] The change in the total surface energy, $\Delta\gamma$, that accompanies the present growth regime should meet the condition:[2,44]

$$\Delta\gamma = \sigma_{b\text{-TiO2}} - (\sigma_{IO} + \gamma_{b\text{-TiO2/IO}}) < 0 \qquad (1)$$

where $\sigma_{b\text{-TiO2}}$ and σ_{IO} are the surface energies of the respective materials (which are affected by surfactant adhesion and/or electronic effects, *e.g.*, related to reconstruction) and $\gamma_{b\text{-TiO2/IO}}$ is the interfacial energy, the latter being mostly related to mismatch-induced strain at the intervening b-TiO_2/IO junction regions. Here, the attainment of bonding b-TiO_2/IO interfaces can be regarded as a process that permits significant compensation for the high $\gamma_{b\text{-TiO2/IO}}$ value by a proportionally larger decrease both in the $\sigma_{b\text{-TiO2}}$ and σ_{IO} terms. Actually, formation of free-standing IO crystalline embryos in a b-TiO_2-loaded IO-generating system could be disfavoured (*i.e.*, leading to an increase in $\Delta\gamma$) due to extreme surface tension that would be associated with tiny IO clusters. Also, the exposed b-TiO_2 NR facets could be destabilized under the particular chemical potential value attained for the IO monomer species in the solution.

From a microscopic point of view, the synthetic versatility achieved here in the engineering of the present b-TiO_2/IO HNCs growth mode should be ultimately correlated with the peculiar structural/morphological features and chemical reactivity offered by the b-TiO_2 NR seeds. Such exclusivity can be better illustrated by comparison with the a-TiO_2 NRs that were employed to grow the aforementioned prototypes of highly strained binary b-TiO_2-IO HNCs.[16] This is discussed as follows.

In the previously reported case of a-TiO_2/IO HNC development, a-TiO_2 seeds were synthesized by a low-temperature (100 °C) hydrolysis route that affords NRs with remarkably smaller dimensions (the short and long axis reached up to about 3–4 nm and 20–30 nm, respectively).[34] The a-TiO_2 NRs were c-axis elongated and enclosed by longitudinal sidewalls made of a characteristic stepped pattern of crystallographically equivalent (011)/(101)-type facets, while less stable (001)-type facets constituted the basal apexes.[17,34,45] The formation of a-TiO_2/IO HNCs involved attainment of rather small and locally curved a-TiO_2/IO heterointerfaces characterized by well-defined lattice coincidence relationships. This fact suggested that IO nucleation could proceed as a means of selectively eliminating high-energy edges on the longitudinal sidewalls of the a-TiO_2 NR seeds. However, constraints imposed by the huge interfacial strain could limit wetting of the (011)/(101) facets underneath the edges, thereby causing dramatic structural distortion across both material domains of the HNCs, as experimentally proven. Also, the degree of IO-induced polarization across each a-TiO_2 NRs should be relevant, owing to the small seed volumes. These factors could jointly account for the inhibition of reiterated deposition events, on one side, and for the observed restriction of IO growth to sizes smaller than ~15–17 nm, on the other side.[16]

As for what regards the present study, the concerned c-axis-elongated b-TiO_2 seeds exhibit uniform shapes and are enclosed by relatively smooth surfaces, comprising a majority of longitudinal (210) facets, and less-extended basal (120)- and (001)-type facets, with a generally low occurrence of asperities, such as edges and corners. Morphology and surface regularity as well as crystalline quality improve for NRs with increasingly larger dimensions due to beneficial contribution of the long reaction times and high temperature (280 °C) at which they are synthesized.[35] Additionally, it is worth noting that, although the dominant (210)-type surfaces in b-TiO_2 NRs are structurally similar to the (011)/(101) facets that prevail in a-TiO_2 NRs, nevertheless slight divergences in the interatomic distances and in arrangements of the fundamental building block can result in distinct reactivities.[46,47] Therefore, IO deposition on b-TiO_2 surface can be expected to proceed with a different efficiency than onto (011)/(101) a-TiO_2 facets. It is conceivable that IO could be kinetically overdriven toward regions of the exposed b-TiO_2 facets where surfactant passivation is temporarily weaker and/or adsorption of solution monomers chemically activates the seeds. Our results indicate that, on proportionally larger b-TiO_2 seeds, hence offering more extended and equally perfected facets, the probability of multiple IO deposition events can be enhanced, provided that the monomer supersaturation at the critical nucleation stage is high enough (note that the latter condition is practically realized by means of calibrated fast precursor injections). As suggested by HRTEM analyses, IO tends to grow non-epitaxially, which is not surprising on the basis of the structural dissimilarly between the spinel cubic and orthorhombic brookite structures. Such growth mode is likely to facilitate IO domains to take a range of lattice orientations with respect to the b-TiO_2 substrate, which could benefit interfacial strain minimization. The rather large junction areas shared by the respective material portions actually prove that IO nucleation and growth on those particular facets which are available on b-TiO_2 seeds is not detrimentally affected by the energy cost for formation of multiple interfaces. In general, it is plausible that elastic repulsions intervening among IO domains implanted on the same seed can be alleviated on

suitably sized NRs on which sufficiently large inter-domain distances can be indeed guaranteed.[48] In such cases, possible charge polarization effects at the relevant heterojunctions are likely to be dissipated across NR sections characterized by high volumes.

3.5 Magnetic properties of the HNCs

The magnetic performances of the newly synthesized heterostructures have been investigated by superconducting quantum interference device (SQUID) magnetometry. The impact of TiO_2/IO oxide heterojunction formation on the resulting properties can be appreciated from the representative cases of study in Fig. 6, where the magnetic properties of HNCs grown from the same NR seeds ($\sim$10 $\times$ 100 nm) and carrying IO domains with different mean sizes ($\sim$7, $\sim$19 and $\sim$25 nm, respectively) are compared (the respective statistical size evaluations can be found in Fig. S4 in the ESI†)

The magnetization curves at 300 K (Fig. 6a) follow a Langevin-type function in all cases. The HNCs with the $\sim$19 and $\sim$25 nm IO domains exhibit a weak ferromagnetic behaviour (as inferred from the low coercive field values, $H_C^{300\ K}$, of 10 Oe and 14 Oe, and remanence ($M_R^{300\ K}$) of 3.2 and 6.7 emu g^{-1}, respectively), while the sample with the $\sim$7 nm IO domains shows superparamagnetic properties, in good agreement with the size dependence documented in the literature for IO NCs synthesized by surfactant-assisted high-temperature routes.[49–53] The low-temperature hysteresis cycles (Fig. 6b) reveal a saturation magnetization at 5 K ($M_S^{5\ K}$) of about $\sim$44, $\sim$25 and $\sim$17 emu g^{-1} with decreasing IO size, respectively, which therefore fall below $M_S^{5\ K}$ for bulk cubic spinel iron oxide (around 80–85 emu g^{-1}). On one hand, it is well known that, in spinel ferrite materials, the presence of a spin disordered and/or frustrated surface layer, whereby the reduced coordination number of surface atoms can favour spin configurations different from the fully aligned one, can lead to a spin-glasslike behaviour causing size-dependent reduction of M_S in nanostructures.[49–53] On the other hand, a comparison with literature data as well as with the behaviour of corresponding physical mixture samples (*i.e.*, made of *b*-TiO_2 NRs and unbound IO NCs), suggests that the aforementioned mechanism cannot fully explain the remarkable reduction in $M_S^{5\ K}$ detected for the present HNCs. One important aspect that should be taken into account is that in these heterostructures there exist direct bonding relationships between IO and TiO_2 at the junctions that are attained. In this respect, it is plausible to assume formation of an interfacial region where IO is characterized by unique compositional/structural features, which could lead to electronic structure modifications and symmetry breaking capable to unusually influence the magnetization values. The ultimate impact could

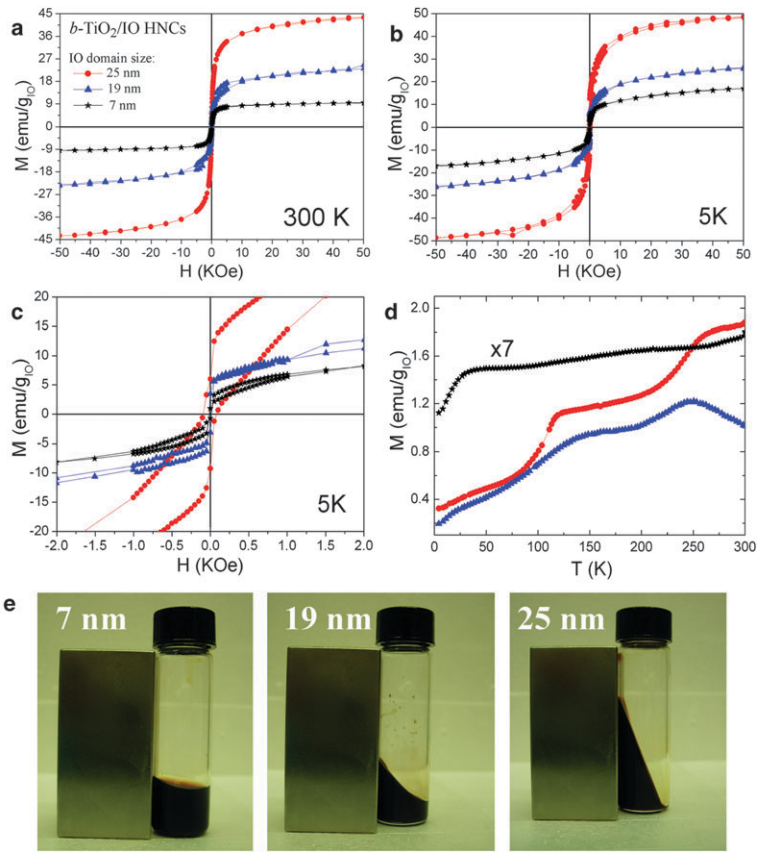

Fig. 6 Comparative analysis of the magnetic properties of *b*-TiO_2/IO HNCs, grown from 8 $\times$ 100 nm sized *b*-TiO_2 NR seeds, which are decorated with IO domains with median sizes of $\sim$7, $\sim$19, $\sim$25 nm, respectively. The Figure panels show: (a) Magnetization curves recorded at 300 K. (b–c) Full and low-field expanded views of the hysteresis loops recorded at 5 K after ZFC from 300 K, respectively. (d) Temperature-dependent magnetization measurements after ZFC. (e) Daylight photographs showing that concentrated colloidal solutions of the HNCs are instantly attracted by a 0.5 T magnet, showing the typical behaviour of ferrofluids, depending on the mean IO domain size.

be expected to be relevant, as the relative interfacial area that the magnetic material shares with the semiconductor is quite large.[2,3,16,43]

A comparative inspection of expanded low-field view of the 5 K hysteresis curves (Fig. 6c) discloses a double-loop behaviour that is marked by a change in the slope of both the ascending and descending branches and by a characteristic kink at low fields. This suggests co-existence of two decoupled phases, a "softer" and a "harder" one, which can switch almost independently. One of such phases could be related to the aforementioned spin-glasslike surface phase of IO, while the other could reflect the magnetocrystalline anisotropy of the ferrimagnetically ordered "core". The fact that the hysteresis curve does not become flat at saturation reflects the progressive alignment of the spin-disordered phase along the external field.[51,52] The magnetic parameters of the two component phases can be estimated by differentiating the hysteresis curves, as described previously.[43b] It is found that the HNCs carrying IO sections of $\sim$7, $\sim$19 and $\sim$25 nm exhibit coercive field values $H^{5\ K}_{C\text{-soft}} \approx$ 25 Oe, 35 Oe and 35 Oe associated to their soft phase contribution, and $H^{5\ K}_{C\text{-hard}} \approx$ 580 Oe, 3720 Oe and 750 Oe for the hard phase component, respectively. These data agree with the expectation that the inner "core" of the IO domain could provide a proportionally higher contribution to the overall magnetic anisotropy relative to its spin-glasslike surface layer, as the IO dimensions become increasingly larger.[49–53]

The thermal dependence of the magnetization in Fig. 6d, that has been examined for the selected samples after zero-field cooling (ZFC), is featured by rather broad curves exhibiting inflection points and relative maxima at about 25 K, at 140 K and 245 K, and at 120 K and 260 K, for the HNCs carrying $\sim$7 nm $\sim$19 nm, and $\sim$25 nm sized IO, respectively. These features can have various origins. The kinks at around 120–140 K can be attributed to the Verwey transition, which is usually related to the presence of stoichiometric magnetite (Fe_3O_4).[54,55] The existence of such crystal phase in relevant proportions is indeed expected for relatively large IO nanoparticles ($>$ 10–12 nm), for which incomplete oxidation results in an inner "core" made of the less oxidized magnetite (*i.e.*, Fe_3O_4) and an outer layer of the more oxidized maghemite (*i.e.*, γ-Fe_2O_3).[49–55] Moreover, it should be considered that the size distributions of the IO domains are relatively broad and quasi-bimodal for the investigated HNCs decorated with the larger IO domains (Fig. S4 in the ESI†). An increased anisotropy could be associated with the formation of the *b*-TiO_2/IO bonding junctions, which could play a role in enhancing the thermal stability of the magnetization, as observed for other types of heterostructures.[2,3,43] In this respect, the presence of heterointerfaces with varying extensions would further contribute to spread the distribution of energy barriers, thus accounting for the ZFC curve broadness with maxima shifted to higher temperature. Overall, these measurements further highlight that the creation of direct junctions between IO domains and *b*-TiO_2 can be effectively used to generate magnetic properties that are distinct from those of the otherwise isolated IO NCs as well as from those of corresponding *b*-TiO_2/IO physical mixtures. The ability to engineer HNCs in which *b*-TiO_2 and IO can be effectively contacted *via* large interfacial areas (*i.e,* in which a substantial surface fraction of IO is shared with TiO_2) appears to be critical in differentiating their behaviour from those of their *a*-TiO_2/IO based counterparts.[16]

Finally, it is worth noting that the as-prepared HNCs can be fully dissolved in organic nonpolar media due to their hydrophobic surfactant capping, resulting in highly concentrated colloidal solutions that behave as ferrofluids. Fig. 6e indeed highlights that HNCs can instantly respond to an applied magnet to an extent that directly depends on the IO size.

4. Conclusions

We have devised a surfactant-assisted seeded-growth approach enabling the synthesis of HNCs individually made of one *b*-TiO_2 rod-like section functionalized with either one or multiple nearly spherical IO domains. The availability of *b*-TiO_2 NRs with tuneable geometric parameters has offered the opportunity to deliberately exploit the size-dependent reactivity of such seeds towards heterogeneous nucleation and growth of iron oxide upon regulating the time-variation of the chemical potential for the monomers in the solution environment. This translates into high versatility in the preparation of HNCs in a variety of topological arrangements, for which the dimensions of the component material domains can be controlled almost independently over a wide dimensional range, circumventing heteroepitaxial growth constraints related to structural dissimilarity between the involved material lattices. Our study suggests that assessment of the genuine impact of the inherent dimensional and structural features of the seeds, and of their interplay with kinetically driven growth processes, could pave the way to an increased level of synthetic sophistication in HNC engineering by means of seeded-growth techniques. More refined characterization studies as well as theoretical modelling are currently underway to elucidate the nature of the heterointerfaces in these HNCs, which appear to be the key for rationalizing the origin of modified magnetic behaviour of IO domains bound to *b*-TiO_2.

Acknowledgements

The authors acknowledge financial support from the Italian Ministry of Research (contract no. RBIN048TSE), from the European Union under the Framework 6 Program under a contract for an Integrated Infrastructure Initiative (Reference 026019 ESTEEM), from the Spanish Ministry of Science and Innovation (project no. FIS2008-06249), and from the Ministerio de Ciencia e Innovacion (project no. MAT2005-06024-C02-01).

References

1 G. A. Ozin, A. C. Arsenault and L. Cademartiri, in *Nanochemistry: A Chemical Approach to Nanomaterials*, RSC Publishing, Cambridge, 2008, p. 850.
2 M. Casavola, R. Buonsanti, G. Caputo and P. D. Cozzoli, *Eur. J. Inorg. Chem.*, 2008, **6**, 837–854.
3 G. Caputo, R. Buonsanti, M. Casavola and P. D. Cozzoli, in *Advanced Wet-Chemical Synthetic Approaches to Inorganic Nanostructures*, ed. P. D. Cozzoli, Transworld Research Network, 2008, pp. 407–453.

4 R. Buonsanti, M. Casavola, G. Caputo and P. D. Cozzoli, *Recent Patents Nanotechnol.*, 2007, **1**, 224–232.
5 P. D. Cozzoli, T. Pellegrino and L. Manna, *Chem. Soc. Rev.*, 2006, **35**, 1195–1208.
6 G. Salazar-Alvarez, J. Sort, S. Suriñach, M. D. Baró and J. Nogués, *J. Am. Chem. Soc.*, 2007, **129**, 9102–9108.
7 O. Masala and R. Seshadri, *J. Am. Chem. Soc.*, 2005, **127**, 9354–9355.
8 J. Li, H. Zeng, S. Sun, J. P. Liu and Z. L. Wang, *J. Phys. Chem. B*, 2004, **108**, 14005–14008.
9 R. He, X. You, J. Shao, F. Gao, B. Pan and D. Cui, *Nanotechnology*, 2007, **18**, 315601.
10 V. Salgueirino-Maceira, M. A. Correa-Duarte, M. Farle, A. Lopez-Quintela, K. Sieradzki and R. Diaz, *Chem. Mater.*, 2006, **18**, 2701–2706.
11 L. Zhang, S. Qiao, Y. Jin, H. Yang, S. Budihartono, F. Stahr, Z. Yan, X. Wang, Z. Hao and G. Q. Lu, *Adv. Funct. Mater.*, 2008, **18**, 3203–3212.
12 T.-J. Yoon, K. N. Yu, E. Kim, J. S. Kim, B. G. Kim, S.-H. Yun, B.-H. Sohn, M.-H. Cho, J.-K. Lee and S. B. Park, *Small*, 2006, **2**, 209–215.
13 S. Rakshit and S. Vasudevan, *ACS Nano*, 2008, **2**, 1473–1479.
14 J. Shin, H. Kim and I. S. Lee, *Chem. Commun.*, 2008, **43**, 5553–5555.
15 C. Cheng, K. F. Yu, Y. Cai, K. K. Fung and N. Wang, *J. Phys. Chem.*, 2007, **111**, 16712–16716.
16 R. Buonsanti, V. Grillo, E. Carlino, C. Giannini, M. L. Curri, C. Innocenti, C. Sangregorio, K. Achterhold, F. G. Parak, A. Agostiano and P. D. Cozzoli, *J. Am. Chem. Soc.*, 2006, **128**, 16953–16970.
17 X. Chen and S. S. Mao, *Chem. Rev*, 2007, **107**, 2891–2959.
18 H. Jung, H. Park, J. Kim, J. H. Lee, H. G. Hur, N. V. Myung and H. Choi, *Environ. Sci. Technol.*, 2007, **41**, 4741–4747.
19 G. Palmisano, V. Augugliaro, M. Pagliaro and L. Palmisano, *Chem. Commun.*, 2007, **33**, 3425–3437.
20 X. Song and L. Gao, *J. Am. Ceram. Soc.*, 2007, **90**, 4015–4019.
21 Y. Ao, J. Xu, D. Fu, X. Shen and C. Yuan, *Sep. Purif. Technol.*, 2008, **61**, 436.
22 C. T. Yavuz, J. T. Mayo, W. W. Yu, A. Prakash, J. C. Falkner, S. Yean, L. Cong, H. J. Shipley, A. Kan, M. Tomson, D. Natelson and V. L. Colvin, *Science*, 2006, **314**, 964–967.
23 L. Gao, J. Zhuang, L. Nie, J. Zhang, Y. Zhang, N. Gu, T. Wang, J. Feng, D. Yang, S. Perrett and X. Yan, *Nat. Nanotechnol.*, 2007, **2**, 577.
24 C. T. Chen and Y. C. Chen, *Anal. Chem.*, 2005, **77**, 5912–5919.
25 Q. A. Pankhurst, J. Connolly, S. K. Jones and J. Dobson, *J. Phys. D*, 2003, **36**, R167–R181.
26 A. Ito, M. Shinkai, H. Honda and T. Kobayashi, *J. Biosci. Bioengineering*, 2006, **100**, 1–11.
27 J. D. G. Durán, J. L. Arias, V. Gallardo and A. V. Delgado, *J. Pharm. Sci.*, 2008, **97**, 2948–2983.
28 Y.-w. Jun, J.-H. Lee and J. Cheon, *Angew. Chem., Int. Ed.*, 2008, **47**, 5122–5135.
29 J.-w. Seo, H. Chung, M.-y. Kim, J. Lee, I.-h. Choi and J. Cheon, *Small*, 2007, **3**, 850–853.
30 T. Paunesku, T. Rajh, G. Wiederrecht, J. Maser, S. Vogt, N. Stojicevic, M. Protic, B. Lai, J. Oryhon, M. Thurnauer and G. Woloschak, *Nat. Mater.*, 2003, **2**, 343–346.
31 D. Beydoun, R. Amal, G. K. C. Low and S. McEvoy, *J. Phys. Chem. B*, 2000, **104**, 4387–4396.
32 X. W. Lou and L. A. Archer, *Adv. Mater.*, 2008, **20**, 1853–1858.
33 S. Abramson, L. Srithammavanh, J.-M. Siaugue, O. Horner, X. Xu and V. Cabuil, *J. Nanopart. Res.*, 2009, **11**, 459–465.
34 P. D. Cozzoli, A. Kornowski and H. Weller, *J. Am. Chem. Soc.*, 2003, **125**, 14539–14548.
35 R. Buonsanti, V. Grillo, E. Carlino, C. Giannini, T. Kipp, R. Cingolani and P. D. Cozzoli, *J. Am. Chem. Soc.*, 2008, **130**, 11223–11233.
36 S. G. Kwon and T. Hyeon, *Acc. Chem. Res.*, 2008, **41**, 1696–1709.
37 B. Schmitt, C. Brönnimann, E. F. Eikenberry, G. Hülsen, H. Toyokawa, R. Horisberger, F. Gozzo, B. Patterson, C. Schulze-Briese and T. Tomizaki, *Nucl. Instrum. Methods Phys. Res., Sect. A*, 2004, **518**, 436–439.
38 A. Altomare, M. C. Burla, C. Giacovazzo, A. Guagliardi, A. G. G. Moliterni, G. Polidori and R. Rizzi, *J. Appl. Crystallogr.*, 2001, **34**, 392–397.
39 A. LeBail and A. Jouanneaux, *J. Appl. Crystallogr.*, 1997, **30**, 265–271.
40 M. J. Hÿtch, E. Snoeck and R. Kilaas, *Ultramicroscopy*, 1998, **74**, 131–146.
41 HRTEM Quantitative Phase Analysis. GPA Phase plug-in for DigitalMicrograph (Gatan) available from HREM Research Inc.: http://www.hremresearch.com.
42 X. Q. Gong and A. Selloni, *Phys. Rev. B*, 2007, **76**, 235307.
43 (*a*) M. Casavola, V. Grillo, E. Carlino, C. Giannini, F. Gozzo, E. Fernandez Pinel, M. A. Garcia, L. Manna, R. Cingolani and P. D. Cozzoli, *Nano Lett.*, 2007, **7**, 1386–1395; (*b*) M. Casavola, A. Falqui, M. A. Garcia, M. E. Garcia-Hernandez, C. Giannini, R. Cingolani and P. D. Cozzoli, *Nano Lett.*, 2009, **9**, 366–376.
44 I. V. Markov, *Crystal Growth for Beginners; Fundamentals of Nucleation, Crystal Growth, and Epitaxy*, World Scientific, Singapore, 2003.
45 G. Caputo, C. Nobile, T. Kipp, L. Blasi, V. Grillo, E. Carlino, L. Manna, R. Cingolani, P. D. Cozzoli and A. Athanassiou, *J. Phys. Chem. C*, 2008, **112**, 701–714.
46 M. Lazzeri, A. Vittadini and A. Selloni, *Phys. Rev. B*, 2001, **63**, 155409.
47 W.-K. Li, X.-Q. Gong, G. Lu and A. Selloni, *J. Phys. Chem. C*, 2008, **112**, 6594–6596.
48 R. D. Robinson, B. S. Denis, O. Demchenko, C. K. Erdonmez, L.-W. Wang and A. P. Alivisatos, *Science*, 2007, **317**, 355–358.
49 S. H. Sun, H. Zeng, D. B. Robinson, S. Raoux, P. M. Rice, S. X. Wang and G. Li, *J. Am. Chem. Soc.*, 2004, **126**, 273–279.
50 F. X. Redl, C. T. Black, G. C. Papaefthymiou, R. L. Sandstrom, M. Yin, H. Zeng, C. B. Murray and S. P. O'Brien, *J. Am. Chem. Soc.*, 2004, **126**, 14583–14599.
51 D. Fiorani, in *Surface Effects in Magnetic Nanoparticles*, Springer, New York, 2005.
52 X. Batlle and A. Labarta, *J. Phys. D.*, 2002, **35**, R15–R42.
53 (*a*) T. N. Shendruk, R. D. Desautels, B. W. Southern and J. van Lierop, *Nanotechnology*, 2007, **18**, 455704; (*b*) T. J. Daou, J. M. Greneche, G. Pourroy, S. Buathong, A. Derory, C. Ulhaq-Bouillet, B. Donnio, D. Guillon and S. Begin-Colin, *Chem. Mater.*, 2008, **20**, 5869–5875.
54 N. Guigue-Millot, N. Keller and P. Perriat, *Phys. Rev. B*, 2001, **64**, 012402.
55 W. Tabis, Z. Tarnawski, Z. Kakol, G. Król, A. Kolodziejczyk, A. Kozlowski and A. Fluerasu, *J. Alloys Compd.*, 2007, **442**, 203–205.